Defect-based interfaces as the essential factor in engineering carbon-nitride-based visible-light-driven Z-scheme photocatalyst

Sicong Wang [1†], Zhenyuan Teng [3†], Yanqi Xu [1], Meng Yuan [1], Yunhao Zhong [1], Sixiao Liu [1], Chengyin Wang [1*], Guoxiu Wang [2], Teruhisa Ohno [3*]

[1] College of Chemistry and Chemical Engineering, Jiangsu Key Laboratory of Environmental Engineering and Monitoring, Yangzhou University, 180 Si-Wang-Ting Road, Yangzhou, 225002, China

[2] Centre for Clean Energy Technology, Faculty of Science, University of Technology Sydney, Sydney, NSW 2007, Australia

[3] Department of Applied Chemistry, Faculty of Engineering, Kyushu Institute of Technology, 1-1 Sensuicho, Tobata, Kitakyushu 804-8550, Japan

*E-mail: wangcy@yzu.edu.cn; tohno@che.kyutech.ac.jp

[†] These authors contributed equally.
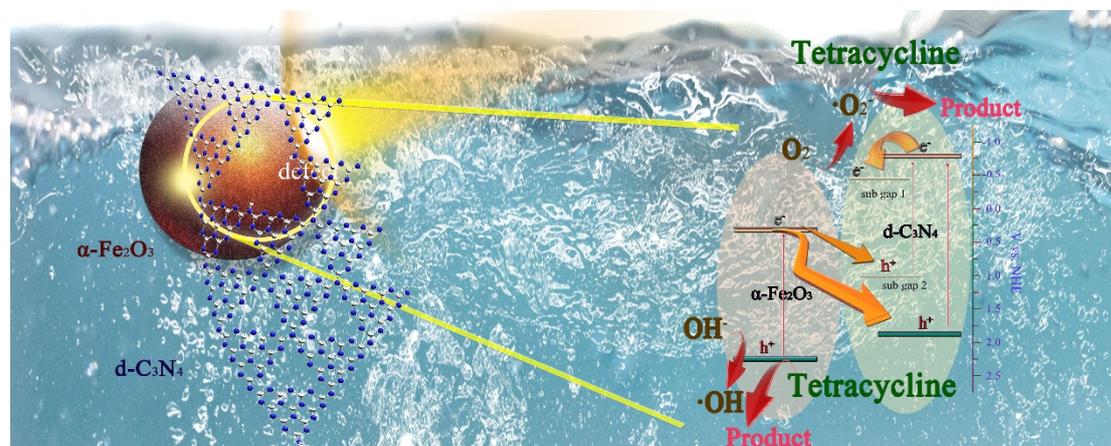
Highlights

• Defect-rich carbon nitride was utilized in Z-scheme systems for the first time.

• The proposed mechanism doubles the activity of traditional Z-scheme photocatalysts.

• The promoted Z-scheme mechanism was verified to have an excellent universality.

Abstract

In designing of carbon nitride-based Z-scheme systems, band structure engineering of graphitic carbon nitride (g-C_3N_4) is unquestionably a crucial demand but paid rare attention to. Here, the broadened light absorption and charge transfer on sub gaps induced by thermal defects in defect-rich carbon nitride (d-C_3N_4) are simultaneously utilized to engineer a novel and more efficient Z-scheme system. The as-prepared α-Fe_2O_3/d-C_3N_4-1 exhibits 8.08, 10.63 and 1.96-fold promotion in the photocatalytic degradation rate for tetracycline compared with g-C_3N_4, d-C_3N_4 and α-Fe_2O_3/g-C_3N_4-1 respectively under visible light. The efficiently restrained charge recombination and broadened light absorption in this Z-scheme system are key parameters of the outstanding photocatalytic activity. This proposed mechanism has the potential to push the limit of traditional carbon-nitride-based Z-scheme photocatalysts and can also shed

substantial light on the engineering strategies for other polymeric Z-scheme photocatalysts.

1. Introduction

Photocatalysis, as one of the most efficient energy conversion pathways, has been under the global spotlight since the Titanium dioxide (TiO_2) was reported by Fujishima and Honda[1]. Over the past few decades, various kinds of efficient photocatalysts were engineered worldwide, such as polymeric materials[2-9], metal oxides[10-15] and metal sulfides[16-20]. Among the recently reported photocatalysts, graphitic carbon nitride ($g-C_3N_4$) is an increasingly prominent one, which is attributed to its low cost, easy preparation and high durability[21-28].

The visible light absorption of $g-C_3N_4$ is still restricted by reason of its large band gap (2.6 - 2.7 eV) and rapid recombination of photo-generated excitons (electrons and holes), which results in the restricted photocatalytic activity under visible light[29, 30]. For purpose of compensating this disadvantage, numerous engineering strategies based on the broadened light absorption and controlled direction of excitons have been extensively investigated, including utilization of surface plasmon resonance (SPR)[31-33], element doping[34-38], introduction of defects[39-41] and formation of heterojunctions[42-45]. As a special kind of heterojunctions, Z-scheme mechanism is a

promising strategy because it promotes the charge separation efficiency and increases the redox potential of the composite[46]. Recently, numerous semiconductors with suitable band structures have been utilized to engineer direct Z-scheme photocatalysts with g-C_3N_4, such as $FeWO_4$[47], Sn_2S_3[48], BiOI[49] and α-Fe_2O_3[50, 51]. However, simply selecting semiconductors whose band structures are well-matched with that of g-C_3N_4 can only contribute finitely to the development of carbon-nitride-based Z-scheme photocatalysts. As g-C_3N_4 is the semiconductor which usually plays the role of photo-generated electrons donator, enhancing its visible-light absorption at the prerequisite of efficient charge separation is doubtlessly a crucial factor when engineering carbon-nitride-based Z-scheme photocatalysts. Unfortunately, strategies focused on engineering the g-C_3N_4 band structure for enhancing its visible-light absorption in carbon-nitride-based Z-scheme systems are rarely reported.

Thermal defects in g-C_3N_4 induced by calcination at an over-high temperature have been proved to benefit the absorption of visible light but restrict the photocatalytic activity[52]. One sub gap tends to generate between the inherent CB and VB of the defect-rich carbon nitride (d-C_3N_4) due to the newly generated –NH/-NH_2 groups in carbon nitride matrix[52]. Photo-generated charge carriers on both of the sub and inherent bands can recombine at –NH/NH_2 group sites[52]. Therefore, these new recombination pathways for charge carriers can result in higher recombination rate of photo-generated excitons, which led to the reduction of photocatalytic performance.

Here, we proposed a rational engineering strategy with an improved direct Z-

scheme mechanism in α-Fe$_2$O$_3$/d-C$_3$N$_4$ composites. Large-sized α-Fe$_2$O$_3$ nanoparticles were utilized to construct interfaces with –NH/-NH$_2$ groups on d-C$_3$N$_4$ surface. The obtained composite was further employed as the photocatalyst for tetracycline (TC) degradation under visible light and exhibited 1.96-fold TC degradation rate compared to α-Fe$_2$O$_3$/g-C$_3$N$_4$ composite. Because of the excellent matching between band edges of α-Fe$_2$O$_3$ and the sub gaps in d-C$_3$N$_4$, an efficient charge separation was achieved in α-Fe$_2$O$_3$/d-C$_3$N$_4$ composite. As far as we know, this is the first time that the thermal defects were utilized in a Z-scheme system which has potential in double the efficiency of traditional Z-scheme based on g-C$_3$N$_4$. This work may not only shed light onto the construction of carbon nitride-based Z-scheme systems but also promote the development of thermal defect utilization in other polymeric materials.

2. Experimental section

2.1 Materials

The reagents are all at analytical grade and used without any treatment before experiments unless otherwise stated. Commercial α-Fe$_2$O$_3$ was offered by Beijing anheng technology Co., Ltd. Commercial CdO, WO$_3$ and V$_2$O$_5$, Tetracycline (TC), dimethyl pyridine N-oxide (DMPO), p-benzoquinone (BQ), triethanolamine (TEOA) and tert-butyl alcohol (TBA) were purchased from Sinopharm Chemical Reagent Co., Ltd. All of the dyes and antibiotics were purchased from Aladdin (China).

2.2 Synthesis of photocatalysts

2.2.1 Synthesis of g-C$_3$N$_4$ and d-C$_3$N$_4$ Typically, 10 g melamine was loaded into a

crucible which was later calcined in a tube furnace at a heating rate of 3 K min^{-1} and maintained at 823 K for 3 h in the air. After the calcination, 4.2 g yellow g-C$_3$N$_4$ was obtained. For the synthesis of d-C$_3$N$_4$, the only difference compared to that of g-C$_3$N$_4$ was the calcination temperature at 913 K.

2.2.2 Synthesis of α-Fe$_2$O$_3$/d-C$_3$N$_4$ heterojunction photocatalyst For the typical synthesis of α-Fe$_2$O$_3$/d-C$_3$N$_4$-1, 10 mg of commercial α-Fe$_2$O$_3$ nanoparticles was dispersed in 5 mL ethanol. Then, the suspension was treated with sonication to further disperse the α-Fe$_2$O$_3$ nanoparticles. Afterwards, 1 mL of the suspension was added into 5 mL ethanol which contained 100 mg d-C$_3$N$_4$, followed by sonication for 15 min. The suspension was then evaporated at 303 K under continuous stirring. Lastly, the dried mixture was loaded in a crucible and then calcined at 573 K in a tube furnace with air as the atmosphere. The obtained product was denoted as α-Fe$_2$O$_3$/d-C$_3$N$_4$-1 because the theoretical mass ratio of α-Fe$_2$O$_3$ in the photocatalyst was 1 %. Systematically, the products prepared with different mass ratio of α-Fe$_2$O$_3$ were denoted as α-Fe$_2$O$_3$/d-C$_3$N$_4$-0.5, α-Fe$_2$O$_3$/d-C$_3$N$_4$-2 and α-Fe$_2$O$_3$/d-C$_3$N$_4$-3 respectively.

2.2.3 Synthesis of α-Fe$_2$O$_3$/g-C$_3$N$_4$-1 Compared to the synthesis of α-Fe$_2$O$_3$/d-C$_3$N$_4$-1, the only difference of α-Fe$_2$O$_3$/d-C$_3$N$_4$-1 preparation process was that the supporting material was g-C$_3$N$_4$ rather than d-C$_3$N$_4$.

2.2.4 Synthesis of V$_2$O$_5$/d-C$_3$N$_4$-1, WO$_3$/d-C$_3$N$_4$-1 and CdO/d-C$_3$N$_4$-1 Compared to the synthesis ofα-Fe$_2$O$_3$/d-C$_3$N$_4$-1, the only difference of V$_2$O$_5$/g-C$_3$N$_4$-1, WO$_3$/g-C$_3$N$_4$-

1 and CdO/g-C_3N_4-1 was that the decoration materials were V_2O_5, WO_3 and CdO rather than α-Fe_2O_3.

2.2.5 Synthesis of d-C_3N_4-560, d-C_3N_4-580, d-C_3N_4-600 and d-C_3N_4-620 The samples d-C_3N_4-560, d-C_3N_4-580, d-C_3N_4-600 and d-C_3N_4-620 were prepared with the same method as d-C_3N_4, the only difference was that the calcination temperature were 833, 853, 873 and 893 K respectively.

2.3 Photocatalytic activities evaluation

In a typical photocatalytic process, 20 mg photocatalysts was added into 50 mL of 20 mg L^{-1} TC aqueous solution, followed by a 30 min adsorption process in the dark. Afterwards, the suspension was irradiated by a Xe lamp (500 W) with a visible-light optical filter (CEL-UVIRCUT400, CEAULIGHT, Beijing). During the evaluation process, 3 mL suspension was taken out from the flask into a 5 mL centrifuge tube every 20 min. After 80 min photocatalytic process, 2 mL TC solution in every centrifuge tube was taken out after centrifugation for detection of TC concentration. TC concentration was detected by the peak intensity at 357 nm with an UV-vis spectrophotometer.

2.4 Characterization

The morphology of materials was observed using a field emission scanning electron microscope (SEM) (Zeiss_Supra55, Carl Zeiss AG). The X-ray diffractometer (XRD) measurements were conducted on an X-ray diffractometer (D8 Advance, BRUKER-

AXS). Fourier transform infrared spectra (FT-IR) were conducted on a Bruker spectrometer (Tensor 27) using KBr pellets. X-ray photoelectron spectroscopy (XPS) data were recorded with an electron spectrometer (ESCALAB250 Xi, Thermo Scientific). The UV-vis diffuse reflectance spectra (DRS) were obtained using a UV-Vis-NIR spectrophotometer (Cary-5000, Varian). The Brunauer-Emmett-Teller (BET) specific surface area (SSA) was measured via nitrogen adsorption-desorption isotherm methods (ASAP 2020 HD88, Micromeritics). ESR signals were recorded with an A300-10 spectrometer (Bruker, Germany). PL and time-resolved PL spectra were recorded on an Edinburgh FLS920 fluorescence spectrometer. Concentrations of the pollutants were measured with an ultrviolet spectrophotometer (Haineng i5). The content of Fe was detected by an Inductively coupled plasma-mass spectrometer (ICP-MS) (Optima 7300 DV). Thermo-gravimetry analysis was conducted on a thermos-gravimetry machine (Pyris 1 TGA).

2.5 Photoelectrochemical measurements

Photocurrent-time, Electrochemical impedance spectra (EIS) and Mott-Schottky (MS) plots were performed in a CH Instruments working electrochemical station (CHI660B, Shanghai Chenhua Co., China). The electrolyte was 0.1 M Na_2SO_4 aqueous solution. Several drops of sample-water mixture whose concentration was 300 mg L^{-1} were dropped onto the surface of ITO glass and then dried under 313 K in a vacuum drying oven over night to prepare the working electrode. The effective area was controlled to be 1 cm^2 on the ITO glass. The photocurrent-time measurement was

carried out under visible light irradiation in a 20 s on-off light cycle.

3. Results and discussion

3.1 Morphologies of photocatalysts

Unlike the bulk morphology of g-C$_3$N$_4$ (Fig. S1), after 30 min calcination at 913 K, d-C$_3$N$_4$ exhibited thinner two-dimensional morphology (Fig. 1A) which was also observed in sample α-Fe$_2$O$_3$/d-C$_3$N$_4$-1 (Fig. 1B). Consequently, according to the BET results (Fig. S2), α-Fe$_2$O$_3$/d-C$_3$N$_4$-1 and d-C$_3$N$_4$ exhibited larger specific surface area (SSA) values than g-C$_3$N$_4$, which can be attributed to the further calcination of α-Fe$_2$O$_3$/d-C$_3$N$_4$-1. The STEM-HADDF image (Fig. 1C) of α-Fe$_2$O$_3$/d-C$_3$N$_4$-1 clearly showed that the α-Fe$_2$O$_3$ particles were distributed on the surface of d-C$_3$N$_4$. The distinct interface could be observed as the white arrow pointed out in HRTEM image (Fig. 1D) of α-Fe$_2$O$_3$/d-C$_3$N$_4$-1. The lattice interplanar spacing of 0.43 and 0.33 nm were corresponded to (214) and (128) planes of α-Fe$_2$O$_3$[53]. According to the EDX mapping results (Fig. 1E to 1H), the clear elements distribution and loading of α-Fe$_2$O$_3$ were confirmed. Thanks to the ultra-stable property of d-C$_3$N$_4$ in both N$_2$ and O$_2$ (Fig. S3) when the calcination temperature is lower than 600 °C, the contents of α-Fe$_2$O$_3$ in all composites were consistent with the theoretical value. In detail, the mass ratios of α-Fe$_2$O$_3$ in different composites were confirmed to be 0.514 %, 0.971 %, 1.892 %, 3.139 % and 1.011 % in α-Fe$_2$O$_3$/d-C$_3$N$_4$-0.5, α-Fe$_2$O$_3$/d-C$_3$N$_4$-1, α-Fe$_2$O$_3$/d-C$_3$N$_4$-2, α-Fe$_2$O$_3$/d-C$_3$N$_4$-3 and α-Fe$_2$O$_3$/g-C$_3$N$_4$-1 respectively by conducting ICP-MS.

3.2 Composition and structure analysis

XRD was conducted to clarify the existence state of α-Fe_2O_3 and carbon nitride. The diffraction pattern at 27.4° corresponded to (002) plane in XRD pattern of g-C_3N_4 showed a shift to 26.9° in d-C_3N_4, and α-Fe_2O_3/d-C_3N_4 composites (Fig. 2A), which is attributed to the increased interplanar space of carbon nitride after calcination at 913 K[54]. Diffraction peaks at 33.2° and 35.5° verified the existence of α-Fe_2O_3 in the composite. The existence of α-Fe_2O_3 and the chemical environment for O and Fe in α-Fe_2O_3/d-C_3N_4-1 were further probed by XPS. In Fe 2p spectrum of α-Fe_2O_3/d-C_3N_4-1, Fe $2p_{3/2}$ peaks at 710.9 and 712.4 eV, together with the satellite peak located at 719.2 eV, clarified the presence of Fe in +3 oxidation state (Fig. 2B)[55]. In addition, in O 1s spectra (Fig. S4) of d-C_3N_4 and α-Fe_2O_3/d-C_3N_4-1, peaks located at 531.5 and 532.6 eV were respectively assigned to C=O and C-O groups generated during the calcination process. Notably, the peak at 529.8 eV in O 1s spectrum of α-Fe_2O_3/d-C_3N_4-1 corresponded to the O in α-Fe_2O_3 lattice, which indicated the presence of α-Fe_2O_3[56].

In order to investigate the interaction of α-Fe_2O_3 and d-C_3N_4. N 1s and Fe 2p spectra of α-Fe_2O_3, d-C_3N_4 and α-Fe_2O_3/d-C_3N_4-1 were analyzed. Compared to the Fe 2p spectrum of α-Fe_2O_3 (Fig. 2B), the peaks at 710.2, 711.6, 723.9 and 724.8 eV showed obvious shifts to larger binding energy. The satellite peak at 719.2 exhibited no shift, indicating that the oxidation state of Fe was not changed. The resolved peaks at 401.5, 399.3 and 399.0 eV in N 1s spectrum of d-C_3N_4 confirmed the existence of amino functions, tertiary N and pyridinc N respectively (Fig. 2C). After the decoration of α-

Fe$_2$O$_3$, the peaks at 401.5 eV and 399.0 eV in N 1s spectrum of d-C$_3$N$_4$ exhibited negative shifts of 0.3 eV and 0.1 eV in N 1s spectrum of α-Fe$_2$O$_3$/d-C$_3$N$_4$-1. The shifts in N 1s spectra was slight compared to shifts in Fe 2p spectra, this could be attributed to the large surface area of d-C$_3$N$_4$ and limited amount of α-Fe$_2$O$_3$.

Theoretically, the shifts toward both larger and smaller binding energy was induced by "electron screening effect": once a heterojunction was formed, a decreased or increased electron concentration contributed to a larger or smaller binding energy because of the enhanced electron screening effect[57]. Therefore, the electron concentrations on d-C$_3$N$_4$ and α-Fe$_2$O$_3$ increased and decreased respectively. This could be attributed to the formation of Z-scheme system where the electrons on the conduction band of d-C$_3$N$_4$ were remained rather than being consumed after a Zeta-like charge recombination pathway. Moreover, the shifts in N 1s and Fe 2p spectra indicated the strong interaction of α-Fe$_2$O$_3$ and d-C$_3$N$_4$, which provided an efficient charge transfer pathway and facilitated the separation of charge carriers[58].

Fourier transformed infrared (FT-IR) was conducted to analyze the influence of both high temperature and α-Fe$_2$O$_3$ loading. As shown in Fig. 2D, all samples showed absorption peaks at between 1200 and 1600 cm^{-1} and an absorption peak at 800 cm^{-1}, which corresponded to tri-s-triazine ring and CN-heterocycles respectively[59]. Notably, absorption peaks between 2900 and 3400 cm^{-1} corresponded to the N-H stretching vibration in spectra measured with d-C$_3$N$_4$ exhibited obviously increased intensity, indicating that more –NH/NH$_2$ groups were generated after calcination at 913

K. Meanwhile, these –NH/NH$_2$ groups were previously testified as thermal defects in carbon nitride plane and can restrict the photocatalytic activity via accelerating the recombination of photo-generated carriers[52]. After the loading of α-Fe$_2$O$_3$ nanoparticles, these peaks become weaker because the vibration of N-H bonds was restrained. Additionally, with the loading of α-Fe$_2$O$_3$ nanoparticles augmenting, the corresponding absorption peaks became increasingly weaker (Fig. 2E), which could be attributed to the increased amount of restrained N-H bonds.

In order to further understand the interface between the thermal defects and the α-Fe$_2$O$_3$ nanoparticles, a possible structure of d-C$_3$N$_4$ was suggested in scheme 1. Compared to N 1s spectrum of g-C$_3$N$_4$ (Fig. S5), the intensity of the peak at 401.5 eV which confirmed the existence of amino groups increased dramatically in N 1s spectrum of d-C$_3$N$_4$, indicating that more –NH/NH$_2$ were generated in d-C$_3$N$_4$. In addition, the O 1s spectra of g-C$_3$N$_4$ and d-C$_3$N$_4$ showed no difference (Fig. S6 and S7), indicating that the thermal defects did not origin from oxygen-containing groups. In consideration of the fact that when comparing the FTIR spectra of g-C$_3$N$_4$ and d-C$_3$N$_4$, no change for peaks of tri-s-triazine rings or CN-heterocycles was observed, segments with several tri-s-triazine units and the relevant defect-contained carbon nitride planes were suggested as the resource of thermal defects. With the generation of these two kinds of products, the concentration of -NH/NH$_2$ groups (shown in scheme 1 with red circles) were supposed to increase, which was in accordance with the FTIR and XPS results.

Based on the above results, interfaces based on thermal defects (-NH/NH$_2$ groups) and α-Fe$_2$O$_3$ were successfully constructed. Unfortunately, the accurate location of the -NH/NH$_2$ groups on the d-C$_3$N$_4$ surface could not be determined, which caused difficulties to the construction of interface between -NH/NH$_2$ groups and α-Fe$_2$O$_3$ nanoparticles. Therefore, the large-sized α-Fe$_2$O$_3$ nanoparticles were utilized to contact with more -NH/NH$_2$ groups on d-C$_3$N$_4$ surface.

3.3 Optical properties

In order to figure out the change in optical properties of the composite material induced by this heterojunction, UV-Vis and PL were conducted. The light absorption of these composites were investigated via UV-Vis spectra (Fig. 3A). The absorption edge of d-C$_3$N$_4$ exhibited a blue-shift compared to that of g-C$_3$N$_4$, which was attributed to the confinement effect associated with the thinner two-dimensional morphology. In visible light region, d-C$_3$N$_4$ showed a better absorption ability compared to g-C$_3$N$_4$, which was attributed to the two sub gaps[52]. This enhanced visible-light absorption was ascribed to the sub gaps in d-C$_3$N$_4$ which contributed to a low-energy (1.9 eV) charge carrier excitation pathway. In detail, because of the generated thermal defects, there were two sub bands at +0.97 V and -0.38 V respectively[52]. Consequently, the broad absorption edge at 550 nm was attributed to the existence of sub gaps. After the introduction of α-Fe$_2$O$_3$, the products α-Fe$_2$O$_3$/d-C$_3$N$_4$-0.5, α-Fe$_2$O$_3$/d-C$_3$N$_4$-1, α-Fe$_2$O$_3$/d-C$_3$N$_4$-2 and α-Fe$_2$O$_3$/d-C$_3$N$_4$-3 exhibited stronger absorption from 450 nm to 800 nm. The estimated band gaps (Fig. S8) of g-C$_3$N$_4$, d-C$_3$N$_4$ and α-Fe$_2$O$_3$ were 2.58,

2.68 and 1.93 eV respectively.

The photo-generated charge carrier separation was investigated in order to evaluate the change in optical properties induced by α-Fe$_2$O$_3$ and sub gaps in d-C$_3$N$_4$[52]. Under excitation at 360 nm, g-C$_3$N$_4$ exhibited a typical luminescence peak at 468 nm. The center of luminescence peak measured with d-C$_3$N$_4$ showed a red shift (Fig. 3B), which indicated the presence of sub gaps in d-C$_3$N$_4$[52, 60]. Notably, peaks at 455 and 510 nm were also observed in PL spectra of d-C$_3$N$_4$, which confirmed the existence of the two sub gaps, as reported previously[52]. In order to further verify the existence of the three peaks at 455, 485 and 510 nm, the PL plot of d-C$_3$N$_4$ was considered as a function and its first-derivative was figured out. As shown in Fig. S9, the first-derivative result showed three distinct inflection points, which was in accordance with the three peaks in PL spectrum. After the loading of α-Fe$_2$O$_3$ nanoparticles, intensities of all the three emission peaks showed obvious decrease compared to d-C$_3$N$_4$, which was ascribed to the inhibited charge carrier recombination of composite materials. This phenomenon indicated that the two sub gaps could also participated in the photocatalytic process. In addition, α-Fe$_2$O$_3$/d-C$_3$N$_4$-1 showed the weakest peak intensity among all samples, demonstrating the most efficient charge separation among all the candidate composites.

3.4 Photocatalytic activity evaluation and electrochemical properties analysis

Fig. 4A shows the performance of photocatalytic TC degradation in presence of g-C$_3$N$_4$, d-C$_3$N$_4$, α-Fe$_2$O$_3$/d-C$_3$N$_4$-0.5, α-Fe$_2$O$_3$/d-C$_3$N$_4$-1, α-Fe$_2$O$_3$/d-C$_3$N$_4$-2, α-Fe$_2$O$_3$/d-C$_3$N$_4$-3 and α-Fe$_2$O$_3$/g-C$_3$N$_4$-1 respectively. The TC degradation rate in the presence of

α-Fe$_2$O$_3$/d-C$_3$N$_4$-1 was the highest, followed by α-Fe$_2$O$_3$/d-C$_3$N$_4$-0.5 and α-Fe$_2$O$_3$/g-C$_3$N$_4$-1. Notably, compared to d-C$_3$N$_4$, g-C$_3$N$_4$ exhibited an obviously higher photocatalytic TC degradation efficiency, which was because of the rapid charge recombination induced by the sub gaps in d-C$_3$N$_4$. The calculated rate constants (Fig. 4B) for α-Fe$_2$O$_3$/d-C$_3$N$_4$-1 was the highest (0.0202 min^{-1}), followed by α-Fe$_2$O$_3$/g-C$_3$N$_4$-1 (0.0103 min^{-1}), α-Fe$_2$O$_3$/d-C$_3$N$_4$-0.5 (0.0100 min^{-1}), α-Fe$_2$O$_3$/d-C$_3$N$_4$-2 (0.0091 min^{-1}), α-Fe$_2$O$_3$/d-C$_3$N$_4$-3 (0.0088 min^{-1}), g-C$_3$N$_4$ (0.0025 min^{-1}) and finally d-C$_3$N$_4$ (0.0019 min^{-1}). For α-Fe$_2$O$_3$/d-C$_3$N$_4$-0.5, the mass ratio of α-Fe$_2$O$_3$ was low, which resulted in the lack of interfaces between α-Fe$_2$O$_3$ and defect groups. When the mass ratio of α-Fe$_2$O$_3$ increased to 2 % and 3 %, α-Fe$_2$O$_3$/d-C$_3$N$_4$-2 and α-Fe$_2$O$_3$/d-C$_3$N$_4$-3 exhibited lower photocatalytic activity compared to α-Fe$_2$O$_3$/d-C$_3$N$_4$-1. This phenomenon could be attributed to the "shield effect" of excessive α-Fe$_2$O$_3$ nanoparticles. The main reason was as follows: (i) the excessive α-Fe$_2$O$_3$ brought down the d-C$_3$N$_4$ surface active sites[61]; (ii) the excessive α-Fe$_2$O$_3$ limited the light absorption because of its opacity and large size[62, 63]. Photocatalytic degradation rate measured with α-Fe$_2$O$_3$/d-C$_3$N$_4$-1 was 8.08, 10.63 and 1.96 times than that measured with g-C$_3$N$_4$, d-C$_3$N$_4$ and α-Fe$_2$O$_3$/g-C$_3$N$_4$-1. Considering the identical concentration of α-Fe$_2$O$_3$ in these two composites and the same synthesis methods of these two composites, the higher photocatalytic activity of α-Fe$_2$O$_3$/d-C$_3$N$_4$-1 can be attributed to the interface between α-Fe$_2$O$_3$ and –NH/NH$_2$ groups on the d-C$_3$N$_4$ surface.

As shown in the results, the peaks at retention time of ~5.3 min which were attributed to TC decreased dramatically after the photocatalytic reaction (Fig. S10).

Moreover, some peaks of intermediates generated with the increasing time of photocatalytic reaction, indicating that the degradation process of TC was complex. According to HPLC-MS spectra of TC, the the product at m/z of 467 was contributed by the combination of TC molecular and Na^+, which was not observed in the spectra of TC after photocatalytic reaction (Fig. S11), indicating the complete decomposition of TC molecule. Based on the results of HPLC-MS spectra, the photocatalytic degradation process of TC was also proposed, as shown in Fig. S12, which was quite similar to the recently reported work[64]. The proposed degradation process of TC was complex, which was consistent with the results of total organic carbon (TOC) test (Fig. S13). The TOC removal percentages over α-Fe_2O_3/d-C_3N_4-1 and α-Fe_2O_3/g-C_3N_4-1were 40.9 % and 21.3 % respectively within 80 min photocatalytic reaction. After 140 min photocatalytic reaction, the TOC removal percentage over α-Fe_2O_3/d-C_3N_4-1 and α-Fe_2O_3/g-C_3N_4-1reached 79.1 % and 36.9 % respectively. This indicated that α-Fe_2O_3/d-C_3N_4-1 was efficient in TC mineralization, which facilitated its application in polluted water treatment[64].

Apart from its prominent photocatalytic activity, α-Fe_2O_3/d-C_3N_4-1 exhibited an outstanding photocatalytic stability with the activity under visible light irradiation maintained 97.1 % after 400 min (5 cycles) test (Fig. S14). Moreover, photocatalytic degradation experiments of RhB, MB and MO were conducted to investigate further applications of α-Fe_2O_3/d-C_3N_4-1. The degradation efficiencies within 80 min of α-Fe_2O_3/d-C_3N_4-1 were 99.1 % (Fig. S15), 97.4 % (Fig. S16) and 94.0 % (Fig. S17) for RhB, MB and MO respectively. These degradation efficiencies were obviously higher

than those measured with α-Fe$_2$O$_3$/g-C$_3$N$_4$-1, indicating the application potential of α-Fe$_2$O$_3$/d-C$_3$N$_4$-1.

In order to analyze the effect of dye-sensitization on the photocatalytic process of α-Fe$_2$O$_3$/d-C$_3$N$_4$-1, serials of experiments under visible light irradiation (Fig. S18) was conducted (all optical conditions and experimental operations were the same as that in *section 2.3 Photocatalytic activities evaluation*). Firstly, when the experiments were conducted in N$_2$ atmosphere, the intensities of signals for MB, MO, RhB and TC in spectrophotometric spectra showed negligible decrease. This indicated that the photo-degradation reactions could be sufficiently inhibited by N$_2$ bubbling, which was reported previously[65], and the slightly decreased signal intensity could be attributed to dye adsorption. Secondly, in order to further guarantee the exclusion of photo-degradation during the dye adsorption process, TEOA was added before bubbling N$_2$ into each testing system to consume h$^+$ generated under visible light irradiation, and the decrease in signal intensities was also ignorable. The negligible decrease of signal intensities under both experimental conditions indicated the weak adsorption of these four kinds of dye on the surface of α-Fe$_2$O$_3$/d-C$_3$N$_4$-1 during the photocatalytic process, which excluded the effect of dye-sensitization on the discussion of photocatalytic mechanism.

Electrochemical impedance spectra (EIS) and chronoamperometric curves were employed to study the optical and electrochemical properties. Obviously, α-Fe$_2$O$_3$/d-C$_3$N$_4$-1 exhibited the highest photocurrent density (Fig. 5A) under visible light

17

irradiation, indicating a distinctly promoted photon to current conversion efficiency. Additionally, the capacitive arc radius (Fig. 5B) measured with α-Fe$_2$O$_3$/d-C$_3$N$_4$-1 was the smallest among all the results, indicating a minimum transfer barrier for photo-generated charge carriers[59]. Therefore, α-Fe$_2$O$_3$/d-C$_3$N$_4$-1 exhibited an outstanding photoelectric capacity.

3.5 Reactive species identification

The roles of active species (Fig. 6A) generated during the photocatalytic process were investigated by respectively adding the trap agents into the experimental solutions under visible light. Obviously, after the addition of benzoquinone, the TC degradation efficiency exhibited an apparent decrease (80.2 %), indicating that $\cdot O_2^-$ radicals were extremely essential to photocatalytic degradation of TC with α-Fe$_2$O$_3$/d-C$_3$N$_4$-1. With the addition of TEOA and TBA, the photocatalytic performance showed decrease of 25.1 % and 21.7 % respectively, which demonstrated that h$^+$ and $\cdot OH$ also played a considerable role. This phenomenon can be ascribed to the different lifetime of $\cdot OH$ and $\cdot O_2^-$. In another word, the lifetime of $\cdot O_2^-$ is longer than that of $\cdot OH$, which gave larger possibility for $\cdot O_2^-$ to react with TC molecules compared to $\cdot OH$ in reaction solution, which contributed to the crucial role of $\cdot O_2^-$ in this photocatalytic system. Moreover, ESR signal intensities of DMPO-$\cdot OH$ (Fig. S19) and DMPO-$\cdot O_2^-$ (Fig. S20) detected in presence of α-Fe$_2$O$_3$/d-C$_3$N$_4$-1 were higher than those detected with d-C$_3$N$_4$ and α-Fe$_2$O$_3$, indicating a higher charge separation and transfer rate in α-Fe$_2$O$_3$/d-C$_3$N$_4$-

1. Notably, in line with the photocatalytic activity, α-Fe$_2$O$_3$/d-C$_3$N$_4$-1 tended to catalyze the generation of $\cdot$OH and $\cdot$O$_2^-$ in a higher rate compared to α-Fe$_2$O$_3$/g-C$_3$N$_4$-1.

For purpose of further understanding the photocatalytic degradation process with α-Fe$_2$O$_3$/d-C$_3$N$_4$-1 and figuring out the effect of defects in d-C$_3$N$_4$, band structures of g-C$_3$N$_4$, d-C$_3$N$_4$ and α-Fe$_2$O$_3$ were investigated by conducting VP-XPS (Fig. S21) and Mott-Schottky method (Fig. S22 and S23). Compared to g-C$_3$N$_4$, VB and CB of d-C$_3$N$_4$ both exhibited a positive shift (Fig. 6B). According to the Mott-Schottky results, the n-type semiconductor property was maintained in d-C$_3$N$_4$. Moreover, the CB and VB of α-Fe$_2$O$_3$ were measured as 0.40 and 2.25 V respectively. Considering levels of $E_{H_2O/\cdot OH}$ (2.33 V vs. RHE) and $E_{OH^-/\cdot OH}$ (1.99 V vs. RHE), the more negative VB level of α-Fe$_2$O$_3$ and d-C$_3$N$_4$ both limited the direct generation of $\cdot$OH from H$_2$O[51]. Consequently, the $\cdot$OH participated in the photocatalytic process were all generated from the OH$^-$ in the water.

3.6 Mechanism exploration

The measured CB level of α-Fe$_2$O$_3$ was 0.40 V, which is more positive than $E_{O_2/\cdot O_2^-}$ (-0.33 V). As shown in Fig. S19 and Fig. S20, obvious DMPO-$\cdot$OH signals were observed in ESR spectrum of α-Fe$_2$O$_3$ while no signal of DMPO-$\cdot$O$_2^-$ was detected. Namely, in a Type II heterojunction, electrons on the CB of α-Fe$_2$O$_3$ (0.4 V) were deficient for $\cdot$O$_2^-$ generation. However, both in ESR spectra of α-Fe$_2$O$_3$/d-C$_3$N$_4$-1 and α-Fe$_2$O$_3$/g-C$_3$N$_4$-1, strong signals of $\cdot$O$_2^-$ were detected, indicating that the electrons were not possible to transfer onto the CB of α-Fe$_2$O$_3$.

Therefore, the photo-generated electrons and holes tended to transfer via a Z-scheme mechanism. In order to verify the type of charge transfer, action spectra under series of monochromatic light irradiation were recorded. As shown in Fig. 7, for α-Fe_2O_3, as the light wavelength decreased from 600 to 400 nm, the photocurrent densities gradually increased. For α-Fe_2O_3/g-C_3N_4-1, the photocurrent exhibited a sudden increase at the wavelength of 450 nm. Considering that the absorption threshold of g-C_3N_4 was about 470 nm, the rapid increase of photocurrent was ascribed to the Z-scheme type charge transfer which could efficiently accelerate the charge separation[66].

Notably, in action spectrum of α-Fe_2O_3/d-C_3N_4-1, the abrupt increase of photocurrent density occurred at the light wavelength of 500 nm, and at the light wavelength of 550 nm, a visible photocurrent increase was recorded. As previously reported, the light absorption between wavelength from 450 to 550 nm was contributed the existence of two sub gaps. Therefore, the obvious Z-scheme type charge transfer in α-Fe_2O_3/d-C_3N_4-1 was contributed by the thermal defects. Namely, the outstanding photocatalytic activity of α-Fe_2O_3/d-C_3N_4-1 originated partly from the Z-scheme charge transfer between CB of α-Fe_2O_3 nanoparticles and sub-gaps in d-C_3N_4 Although the light-absorption ability of d-C_3N_4, according to the UV-vis results, was weaker than that of g-C_3N_4 at the wavelength of 400 nm, the larger photocurrent density measured with α-Fe_2O_3/d-C_3N_4-1 under irradiation of 400 nm monochromatic light could be contributed by the more efficient charge separation and the faster charge transfer. Therefore, charges in both in α-Fe_2O_3/d-C_3N_4-1 and α-Fe_2O_3/g-C_3N_4-1 transferred via

Z-scheme mechanism.

For the purpose of further elucidating the essential role of thermal defects in α-Fe$_2$O$_3$/d-C$_3$N$_4$ Z-scheme photocatalysts, defect-rich carbon nitride prepared by calcination under gradient temperatures were employed. Obviously, increasing intensities of peaks at from 2900 to 3400 cm^{-1} in FT-IR spectra (Fig. S24) of d-C$_3$N$_4$-560, d-C$_3$N$_4$-580, d-C$_3$N$_4$-600 and d-C$_3$N$_4$-620 indicated the augmentation of the –NH/NH$_2$ groups in carbon nitride matrix. After composited with 1% (mass ratio) α-Fe$_2$O$_3$ nanoparticles, these composites were employed to conduct series of photocatalytic TC degradation experiments. As shown in Fig. S25, the sequence of photocatalytic activity from high to low is: α-Fe$_2$O$_3$/d-C$_3$N$_4$-620, α-Fe$_2$O$_3$/d-C$_3$N$_4$-600, α-Fe$_2$O$_3$/d-C$_3$N$_4$-580 and α-Fe$_2$O$_3$/d-C$_3$N$_4$-560, which agreed with the respective variation tendency of –NH/NH$_2$ amount.

Consequently, a novel Z-scheme mechanism was proposed for α-Fe$_2$O$_3$/d-C$_3$N$_4$ photocatalyst (Fig. 8) on the following basis: i) The PL spectrum of d-C$_3$N$_4$ showed three emission peaks which indicated the charge recombination pathways induced by the two sub gaps. After loading α-Fe$_2$O$_3$ particles, intensities of all the three peaks decreased, indicating the three charge recombination pathways were sufficiently inhibited. ii) The action spectrum of α-Fe$_2$O$_3$/d-C$_3$N$_4$-1 showed abrupt increase at longer light wavelength compared to α-Fe$_2$O$_3$/g-C$_3$N$_4$-1. iii) the photocatalytic activity gradually increased with the amount of thermal defects in d-C$_3$N$_4$. Therefore, for α-Fe$_2$O$_3$/d-C$_3$N$_4$-1, under irradiation of visible light, electrons were excited to the CB of

α-Fe$_2$O$_3$ and d-C$_3$N$_4$ and one sub gap band of d-C$_3$N$_4$, leaving holes on the VB of α-Fe$_2$O$_3$ and d-C$_3$N$_4$ and one sub gap band of d-C$_3$N$_4$. The electrons on CB of α-Fe$_2$O$_3$ then combined with hole on VB and one sub gap band of d-C$_3$N$_4$, leading to a sufficient charge separation. As a result, electrons on CB of d-C$_3$N$_4$ transferred onto the sub gap band and catalyzed the photocatalytic reaction and the holes on the VB of α-Fe$_2$O$_3$ also participated in the catalyzing process.

3.7 Investigation of mechanism universality

Universality is indispensable when evaluating a Z-scheme photocatalytic mechanism. Therefore, besides α-Fe$_2$O$_3$, semiconductors CdO, V$_2$O$_5$ and WO$_3$ were employed to decorate d-C$_3$N$_4$, which was identified by typical peaks in XRD patterns (Fig. S26). The decrease in peak intensities between 2900 and 3400 cm^{-1} in FT-IR spectra of CdO/d-C$_3$N$_4$-1, WO$_3$/d-C$_3$N$_4$-1 and V$_2$O$_5$/d-C$_3$N$_4$-1 revealed their respective contact with –NH/NH$_2$ groups (Fig. S27). The obtained composites were used as the photocatalyst for TC degradation. The Pseudo-first-order kinetics obtained in the presence of these d-C$_3$N$_4$-based composites were obviously higher than those with g-C$_3$N$_4$-based ones (Fig. 9), which demonstrated an outstanding universality of the proposed Z-scheme mechanism.

Therefore, via the proposed mechanism, the enhanced visible-light absorption contributed by the sub gaps in d-C$_3$N$_4$ was rationally utilized while the charge

recombination induced by the two sub gaps was efficiently suppressed, which contributed to a nearly multiplying photocatalytic activity compared to traditional g-C_3N_4-based Z-scheme photocatalysts.

4. Conclusion

In conclusion, this paper pioneered the methodology to engineer a series of Z-scheme photocatalysts based on thermal defects in d-C_3N_4 and systematically investigated their activity and mechanism for photocatalytic TC degradation. Compared to the traditional Z-scheme photocatalysts based on g-C_3N_4, the proposed Z-scheme system showed dramatically improved photocatalytic performance, which is predominately contributed by the broadened light absorption and the accelerated charge separation resulted from the two sub gaps in d-C_3N_4. Notably, the proved outstanding universality makes the proposed mechanism feasible in various Z-scheme systems. This finding not only gives rise to a profound understanding in photocatalytic process with the as-prepared composites but also opens up new possibilities for significantly boosting photocatalytic activity of carbon nitride-based and other polymeric Z-scheme photocatalysts.

instruments and equipment (BZ 201409).

References

[1] A. Fujishima, K. Honda, Nature (London) 238 (1972) 37-38.

[2] X. Wang, S. Blechert, M. Antonietti, ACS Catal. 2 (2012) 1596-1606.

[3] Y. Hou, A.B. Laursen, J. Zhang, G. Zhang, Y. Zhu, X. Wang, S. Dahl, I. Chorkendorff, Angew. Chem., Int. Ed. 52 (2013) 3621-3625.

[4] Y. Zhi, S. Ma, H. Xia, Y. Zhang, Z. Shi, Y. Mu, X. Liu, Appl. Catal., B 244 (2019) 36-44.

[5] X. Chen, J. Zhang, X. Fu, M. Antonietti, X. Wang, J. Am. Chem. Soc. 131 (2009) 11658-11659.

[6] M. Shalom, S. Inal, C. Fettkenhauer, D. Neher, M. Antonietti, J. Am. Chem. Soc. 135 (2013) 7118-7121.

[7] C.M. Aitchison, R.S. Sprick, A.I. Cooper, J. Mater. Chem. A 7 (2019) 2490-2496.

[8] S. Bandyopadhyay, A.G. Anil, A. James, A. Patra, ACS Appl. Mater. Interfaces 8 (2016) 27669-27678.

[9] A.C. Pradhan, T. Uyar, ACS Appl. Mater. Interfaces 9 (2017) 35757-35774.

[10] H. Zeng, W. Cai, P. Liu, X. Xu, H. Zhou, C. Klingshirn, H. Kalt, ACS Nano 2 (2008) 1661-1670.

[11] H. Zheng, J.Z. Ou, M.S. Strano, R.B. Kaner, A. Mitchell, K. Kalantar-zadeh, Adv. Funct. Mater. 21 (2011) 2175-2196.

[12] M. Miyauchi, A. Nakajima, T. Watanabe, K. Hashimoto, Chem. Mater. 14 (2002) 2812-2816.

[13] J. Zhang, Z. Xiong, X.S. Zhao, J. Mater. Chem. 21 (2011) 3634-3640.

[14] M. Pirhashemi, A. Habibi-Yangjeh, S. Rahim Pouran, J. Ind. Eng. Chem. (Amsterdam, Neth.) 62 (2018) 1-25.

[15] M. Shekofteh-Gohari, A. Habibi-Yangjeh, M. Abitorabi, A. Rouhi, Crit. Rev. Environ. Sci. Technol. 48 (2018) 806-857.

[16] J. Chen, X.-J. Wu, L. Yin, B. Li, X. Hong, Z. Fan, B. Chen, C. Xue, H. Zhang, Angew. Chem., Int. Ed. 54 (2015) 1210-1214.

[17] H. Tada, M. Fujishima, H. Kobayashi, Chem. Soc. Rev. 40 (2011) 4232-4243.

[18] J. Yang, H. Yan, X. Wang, F. Wen, Z. Wang, D. Fan, J. Shi, C. Li, J. Catal. 290 (2012) 151-157.

[19] S. Ma, K. Chen, Y.-H. Qiu, L.-L. Gong, G.-M. Pan, Y.-J. Lin, Z.-H. Hao, L. Zhou, Q.-Q. Wang, J. Mater. Chem. A 7 (2019) 3408-3414.

[20] J. Ran, G. Gao, F.-T. Li, T.-Y. Ma, A. Du, S.-Z. Qiao, Nat. Commun. 8 (2017) 13907.

[21] M. Mousavi, A. Habibi-Yangjeh, S.R. Pouran, J. Mater. Sci.: Mater. Electron. 29 (2018) 1719-1747.

[22] Q. Liang, Z. Li, Z.-H. Huang, F. Kang, Q.-H. Yang, Adv. Funct. Mater. 25 (2015) 6885-6892.

[23] Y. Kang, Y. Yang, L.-C. Yin, X. Kang, G. Liu, H.-M. Cheng, Adv. Mater. (Weinheim, Ger.) 27 (2015) 4572-4577.

[24] P. Niu, L.-C. Yin, Y.-Q. Yang, G. Liu, H.-M. Cheng, Adv. Mater. (Weinheim, Ger.) 26 (2014) 8046-8052.

[25] A. Habibi-Yangjeh, M. Mousavi, Adv. Powder Technol. 29 (2018) 1379-1392.

[26] S. Asadzadeh-Khaneghah, A. Habibi-Yangjeh, D. Seifzadeh, J. Taiwan Inst. Chem. Eng. 87 (2018) 98-111.

[27] S. Asadzadeh-Khaneghah, A. Habibi-Yangjeh, K. Nakata, J. Photochem. Photobiol., A 374 (2019) 161-172.

[28] A. Habibi-Yangjeh, M. Mousavi, K. Nakata, J. Photochem. Photobiol., A 368 (2019) 120-136.

[29] S. Cao, J. Low, J. Yu, M. Jaroniec, Adv. Mater. (Weinheim, Ger.) 27 (2015) 2150-2176.

[30] W.-J. Ong, L.-L. Tan, Y.H. Ng, S.-T. Yong, S.-P. Chai, Chem. Rev. (Washington, DC, U. S.) 116 (2016) 7159-7329.

[31] Y. Yang, Y. Guo, F. Liu, X. Yuan, Y. Guo, S. Zhang, W. Guo, M. Huo, Appl. Catal., B 142-143 (2013) 828-837.

[32] F. Dong, Z. Zhao, Y. Sun, Y. Zhang, S. Yan, Z. Wu, Environ. Sci. Technol. 49 (2015) 12432-12440.

[33] X. Wei, C. Shao, X. Li, N. Lu, K. Wang, Z. Zhang, Y. Liu, Nanoscale 8 (2016) 11034-11043.

[34] Y.-P. Zhu, T.-Z. Ren, Z.-Y. Yuan, ACS Appl. Mater. Interfaces 7 (2015) 16850-16856.

[35] T. Xiong, W. Cen, Y. Zhang, F. Dong, ACS Catal. 6 (2016) 2462-2472.

[36] J. Li, B. Shen, Z. Hong, B. Lin, B. Gao, Y. Chen, Chem. Commun. (Cambridge, U. K.) 48 (2012) 12017-12019.

[37] J. Ran, T.Y. Ma, G. Gao, X.-W. Du, S.Z. Qiao, Energy Environ. Sci. 8 (2015) 3708-3717.

[38] J. Hong, X. Xia, Y. Wang, R. Xu, J. Mater. Chem. 22 (2012) 15006-15012.

[39] Q. Tay, P. Kanhere, C.F. Ng, S. Chen, S. Chakraborty, A.C.H. Huan, T.C. Sum, R. Ahuja, Z. Chen, Chem. Mater. 27 (2015) 4930-4933.

[40] P. Niu, G. Liu, H.-M. Cheng, J. Phys. Chem. C 116 (2012) 11013-11018.

[41] V.W.-h. Lau, I. Moudrakovski, T. Botari, S. Weinberger, M.B. Mesch, V. Duppel, J. Senker, V. Blum, B.V. Lotsch, Nat. Commun. 7 (2016) 12165.

[42] M. Xu, L. Han, S. Dong, ACS Appl. Mater. Interfaces 5 (2013) 12533-12540.

[43] J. Zhang, Y. Wang, J. Jin, J. Zhang, Z. Lin, F. Huang, J. Yu, ACS Appl. Mater. Interfaces 5 (2013) 10317-10324.

[44] L. Ge, C. Han, J. Liu, Appl. Catal., B 108-109 (2011) 100-107.

[45] S. Kumar, T. Surendar, A. Baruah, V. Shanker, J. Mater. Chem. A 1 (2013) 5333-5340.

[46] Y. Hong, Y. Jiang, C. Li, W. Fan, X. Yan, M. Yan, W. Shi, Appl. Catal., B 180 (2016) 663-673.

[47] R. Bhosale, S. Jain, C.P. Vinod, S. Kumar, S. Ogale, ACS Appl. Mater. Interfaces 11 (2019) 6174-6183.

[48] Y. Huo, J. Zhang, K. Dai, Q. Li, J. Lv, G. Zhu, C. Liang, Appl. Catal., B 241 (2019) 528-538.

[49] Y. Gong, X. Quan, H. Yu, S. Chen, H. Zhao, Appl. Catal., B 237 (2018) 947-956.

[50] Z. Jiang, W. Wan, H. Li, S. Yuan, H. Zhao, P.K. Wong, Adv. Mater. (Weinheim,

Ger.) 30 (2018) n/a.

[51] J. Wang, X. Zuo, W. Cai, J. Sun, X. Ge, H. Zhao, Dalton Trans. 47 (2018) 15382-15390.

[52] P. Wu, J. Wang, J. Zhao, L. Guo, F.E. Osterloh, J. Mater. Chem. A 2 (2014) 20338-20344.

[53] L. Chen, X. Yang, J. Chen, J. Liu, H. Wu, H. Zhan, C. Liang, M. Wu, Inorg. Chem. 49 (2010) 8411-8420.

[54] J. Xu, Y. Li, S. Peng, G. Lu, S. Li, Phys. Chem. Chem. Phys. 15 (2013) 7657-7665.

[55] S. Yan, Y. Shi, Y. Tao, H. Zhang, Chem. Eng. J. (Amsterdam, Neth.) 359 (2019) 933-943.

[56] Y. Wu, H. Wang, Y. Sun, T. Xiao, W. Tu, X. Yuan, G. Zeng, S. Li, J.W. Chew, Appl. Catal., B 227 (2018) 530-540.

[57] Z. Zhang, K. Liu, Z. Feng, Y. Bao, B. Dong, Sci. Rep. 6 (2016) 19221.

[58] W. Yu, J. Chen, T. Shang, L. Chen, L. Gu, T. Peng, Appl. Catal., B 219 (2017) 693-704.

[59] Z. Teng, H. Lv, C. Wang, H. Xue, H. Pang, G. Wang, Carbon 113 (2017) 63-75.

[60] H.-B. Fang, X.-H. Zhang, J. Wu, N. Li, Y.-Z. Zheng, X. Tao, Appl. Catal., B 225 (2018) 397-405.

[61] Q. Wang, G. Yun, Y. Bai, N. An, Y. Chen, R. Wang, Z. Lei, W. Shangguan, Int. J. Hydrogen Energy 39 (2014) 13421-13428.

[62] X. Chen, S. Shen, L. Guo, S.S. Mao, Chem. Rev. (Washington, DC, U. S.) 110 (2010) 6503-6570.

[63] Y. Xu, C. Du, J.D. Steinkruger, C. Zhou, S. Yang, J. Mater. Sci. 54 (2019) 6930-6942.

[64] J. Bai, Y. Li, P. Wei, J. Liu, W. Chen, L. Liu, Small 15 (2019) n/a.

[65] T. Wang, W. Quan, D. Jiang, L. Chen, D. Li, S. Meng, M. Chen, Chem. Eng. J. (Amsterdam, Neth.) 300 (2016) 280-290.

[66] J. Wang, C. Qin, H. Wang, M. Chu, A. Zada, X. Zhang, J. Li, F. Raziq, Y. Qu, L. Jing, Appl. Catal., B 221 (2018) 459-466.

Figure captions

Fig.1. TEM images of (A) g-C_3N_4, (B) d-C_3N_4 and (C) α-Fe_2O_3/d-C_3N_4-1; (D) HRTEM image of the loaded α-Fe_2O_3 nanoparticles; (E-H) EDX mapping of α-Fe_2O_3/d-C_3N_4-1.

Fig.2. (A) XRD patterns of the materials. (B) Fe 2p XPS spectrum of in d-C_3N_4 and α-Fe_2O_3/d-C_3N_4-1. (C) N 1s spectra of d-C_3N_4 and α-Fe_2O_3/d-C_3N_4-1. (D) FT-IR spectra and (E) Normalized and partially magnified FT-IR spectra of the materials.

Scheme 1. Proposed structure of defects.

Fig.3. (A) UV-Vis adsorption spectra of the prepared materials. (B) PL spectra of the prepared materials.

Fig.4. (A) Photocatalytic TC degradation activity results. (B) Pseudo-first-order kinetics curves calculated with photocatalytic reaction results.

Fig.5. (A) Chronoamperometric curves and (B) EIS results measured with g-C_3N_4, d-C_3N_4, α-Fe_2O_3/g-C_3N_4-1 and α-Fe_2O_3/d-C_3N_4 composites.

Fig.6. (A) Radical scavenger experiments conducted with BQ, TEOA and TBA. (B)

Diagram of CB and VB levels in g-C$_3$N$_4$, d-C$_3$N$_4$ and α-Fe$_2$O$_3$.

Fig.7. Action spectra measured under monochromatic light at wavelength of 650, 600, 550, 500, 450 and 400 nm.

Fig.8. Diagram of the proposed photocatalytic TC degradation mechanism under visible light.

Fig.9. Comparison of photocatalytic TC degradation kinetics.

Fig.1
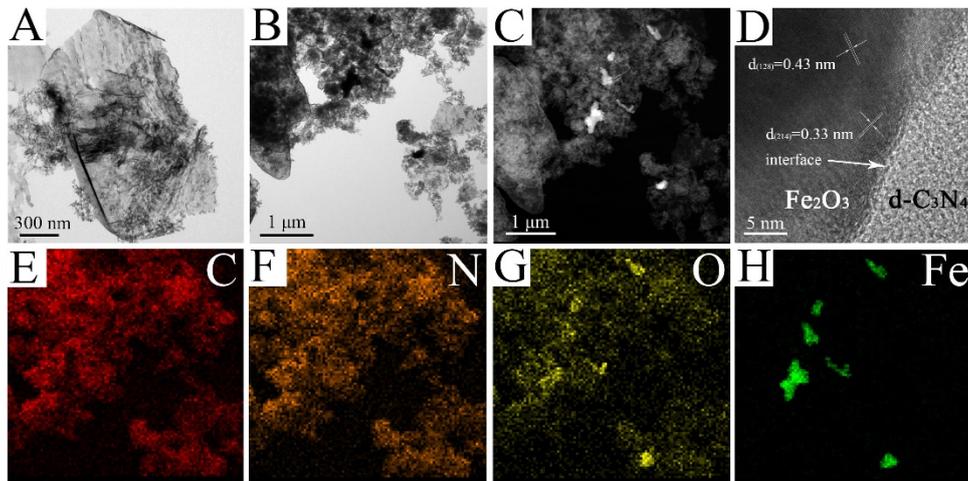
Fig.2
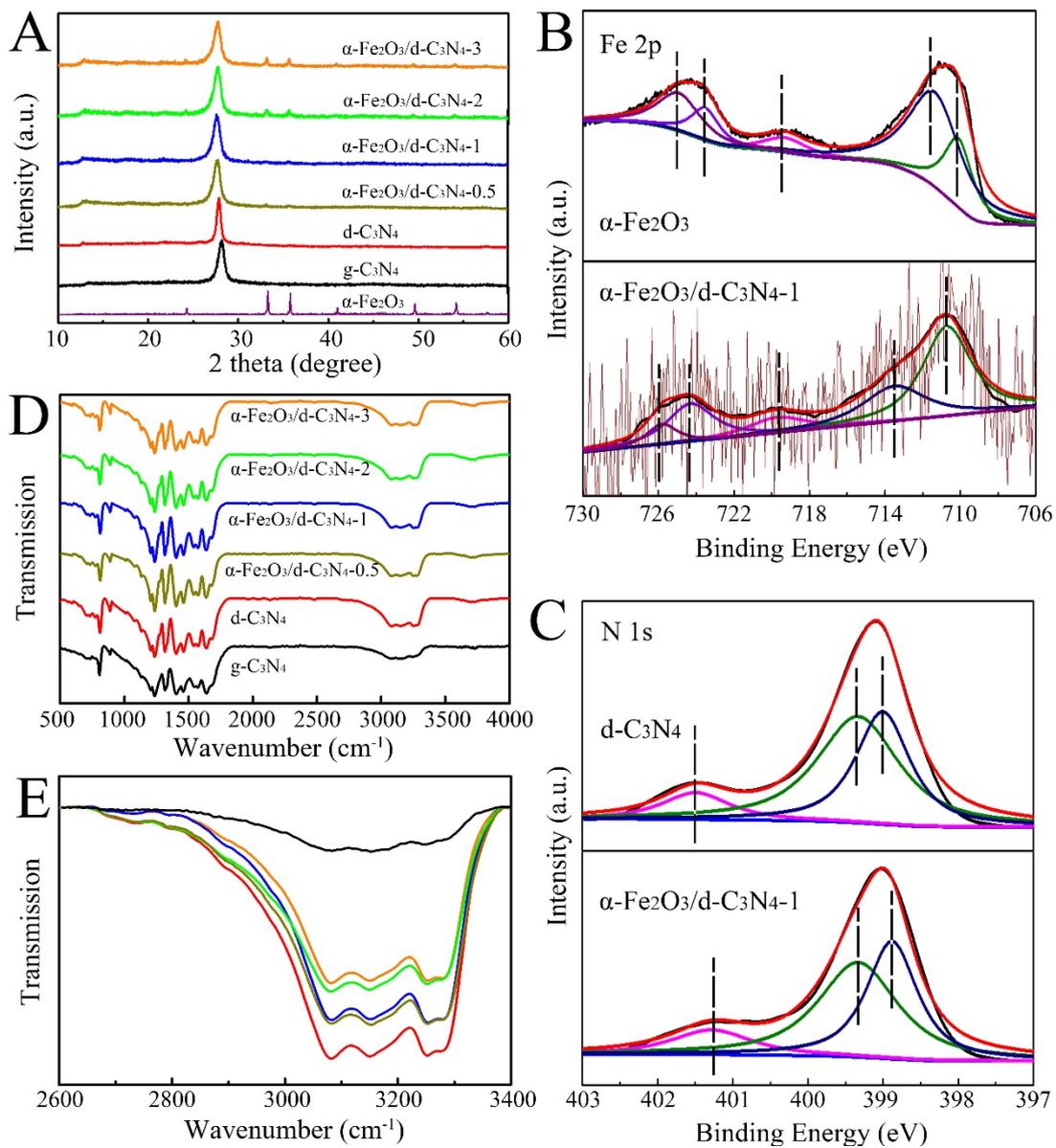
Scheme.1
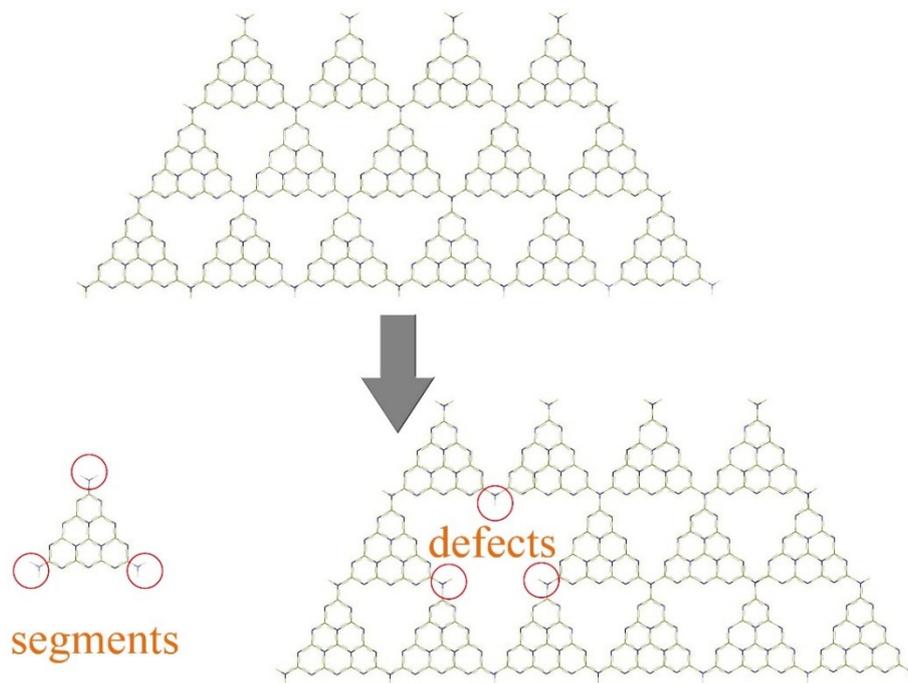
Fig.3
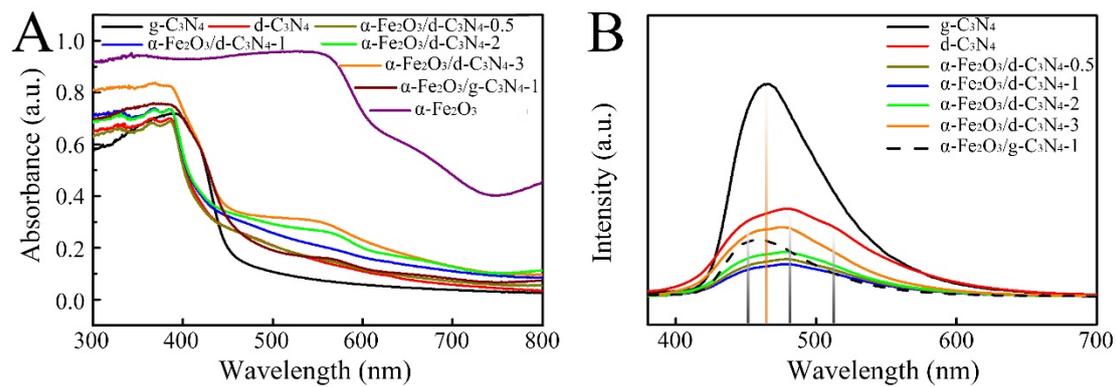
Fig.4

Fig.5

Fig.6

Fig.7

Fig.8

Fig.9